Chemical Engineering Journal 483 (2024) 149230

Contents lists available at ScienceDirect

Chemical Engineering Journal

journal homepage: www.elsevier.com/locate/cej

Confined MOF pyrolysis within mesoporous SiO_2 core–shell nanoreactors for superior activity and stability of electro-Fenton catalysts

Jingwen Wang [a], Hao Li [b], Pan Xia [a], Huanbin Liu [a], Xi Chen [a], Zhihong Ye [a,*], Qiang He [a], Ignasi Sirés [c,*]

[a] Key Laboratory of the Three Gorges Reservoir Region's Eco-Environment, Ministry of Education, College of Environment and Ecology, Chongqing University, Chongqing 400045, China
[b] School of Chemistry and Chemical Engineering, Jiangsu University, Zhenjiang 212013, Jiangsu, China
[c] Laboratori d'Electroquímica dels Materials i del Medi Ambient, Departament de Ciència de Materials i Química Física, Secció de Química Física, Facultat de Química, Universitat de Barcelona, Martí i Franquès 1-11, 08028 Barcelona, Spain

ARTICLE INFO

Keywords:
Core-shell catalyst
Heterogeneous electro-Fenton
Metal leaching
Metal-organic framework
Water treatment

ABSTRACT

Despite the high density and uniform distribution of active sites in metal–organic frameworks (MOFs) and their derivatives, the relatively low stability in water still limits their utilization in heterogeneous catalysis. Herein, the confinement of pyrolyzed MIL-88B(Fe) derivatives within mesoporous SiO_2 allowed fabricating core–shell nanoreactors (Fe/C@mSiO_2) that served as heterogeneous electro-Fenton (HEF) catalysts for the first time, revealing an excellent performance. The as-prepared catalysts were featured by high specific surface area and dense active sites. During service as core–shell nanoreactors, they behaved as a dual function adsorbent-catalyst, exhibiting superior catalytic activity and recyclability as compared to HEF catalysts without shell. Using 0.2 g/L of catalyst, the complete removal of bisphenol A at pH 6.2 and 100 mA was achieved at 120 min, with extremely low iron leaching of 0.11 mg/L. The rigid mSiO_2 shell not only protected the iron active sites from leaching, but it also provided porous and permeable channels for efficient mass transport. The unique core–shell architecture concentrates the catalytic sites and reactants within a confined space, promoting the fast degradation of bisphenol A. Furthermore, the defect-rich carbon substrate and the high dispersibility of iron-rich sites favor a fast electron transfer. The efficient treatment of several organic micropollutants in consecutive trials corroborated the high activity and stability of the Fe/C@mSiO_2. This work contributes to the rational design of HEF catalysts, aiming at consolidating their practical application in advanced wastewater treatment.

1. Introduction

In recent years, the electro-Fenton (EF) process has emerged as one of the most powerful technologies for the treatment of hazardous and persistent organic micropollutants, such as pharmaceuticals and personal care products or pesticides [1–4]. The basic configuration of homogeneous EF systems includes: (i) The in-situ production of H_2O_2 via two-electron oxygen reduction reaction (1), most usually at a carbonaceous cathode; (ii) the continuous activation of H_2O_2 by Fe^{2+} catalyst, according to Fenton's reaction (2), which generates highly oxidizing hydroxyl radical ($^{\bullet}OH$); (iii) the cathodic regeneration of Fe^{2+} via reaction (3); and (iv) the oxidation of water at the anode surface (M) to yield adsorbed M($^{\bullet}OH$) (reaction (4)) [5,6]. The as-formed $^{\bullet}OH$ and M($^{\bullet}OH$) trigger the efficient degradation of pollutants. However, remarkable challenges to scale-up the traditional EF process still persist, as for example the need for acidic conditions ($2.5 < pH < 3.5$) to prevent the iron precipitation, as well as the strict dependence of the efficiencies of reactions (3) and (4) on the catalytic properties of the electrodes [7,8].

$$O_2(g) + 2H^+ + 2\,e^- \rightarrow H_2O_2 \quad (1)$$

$$Fe^{2+} + H_2O_2 \rightarrow Fe^{3+} + {}^{\bullet}OH + OH^- \quad (2)$$

$$Fe^{3+} + e^- \rightarrow Fe^{2+} \quad (3)$$

$$M + H_2O \rightarrow M(^{\bullet}OH) + H^+ + e^- \quad (4)$$

The utilization of transition metals-based solid materials as the Fenton's catalysts, which gives rise to the so-called heterogeneous EF (i.

* Corresponding authors.
E-mail addresses: yezhihong@cqu.edu.cn (Z. Ye), i.sires@ub.edu (I. Sirés).

https://doi.org/10.1016/j.cej.2024.149230
Received 28 August 2023; Received in revised form 9 December 2023; Accepted 29 January 2024
Available online 30 January 2024

e., HEF) process, is expected to minimize the aforementioned disadvantages, extending the operation pH range from acidic to near-neutral or even alkaline and reducing the dependence of EF performance on the efficiencies of reactions (3) and (4) [9]. When solid catalysts are employed, the H_2O_2 decomposition mainly occurs at the liquid–solid interface. The efficiency of H_2O_2 mass transport to the catalyst surface and the availability of metal active sites for H_2O_2 activation determine the $^{\bullet}OH$ production rate, thereby affecting the degradation efficiency of organic pollutants. On the other hand, the reductive recycling of high-valence metal sites of solid catalyst is fulfilled by Fenton-like reaction (5), which prevails over homogeneous reaction (3). Unfortunately, reductive regeneration is usually the rate-limiting step in HEF, regardless of the catalyst nature [10,11]. Within this context, an excellent HEF catalyst must favor mass transport, show high activity and allow fast regeneration of reduced metal active sites, which becomes challenging for catalyst design.

$$M^{(m+n)+} + m\ H_2O_2 \rightarrow M^{n+} + m\ HO_2^{\bullet} + m\ H^+ \quad (5)$$

Recently, metal–organic frameworks (MOFs) have been developed as potentially efficient HEF catalysts because they combine key characteristics such as large surface area, tunable porosity, abundance of active sites and easy functionalization [3,12,13]. Nonetheless, the direct utilization of MOFs for applications in aqueous media is not advisable because they suffer from poor stability, which causes metal leaching and surface deactivation [14,15]. These drawbacks may be addressed by using the MOFs as precursors to fabricate metal/carbon hybrids through a relatively simple pyrolysis approach [16,17]. Several advantages of pyrolyzed MOFs as HEF catalysts can be mentioned: (1) The organic ligands used for MOFs synthesis are transformed into hierarchical porous carbon upon pyrolysis; this results in rich micro/nanopore channels in the carbon matrix, which offer robust sites for metal loading and allow fast charge transfer and mass transport during the HEF treatment [18]; (2) the carbon matrix can catalyze the Fe(III)-to-Fe(II) recycling by decreasing the reduction overpotential [19]; (3) the thermal treatment of MOFs induces changes in the valence of metal sites, thus creating a higher amount of unsaturated metal active sites that ease the occurrence of Fenton's reaction [20]; (4) the pyrolytic derivatives largely inherit the properties of precursors, such as the tailored porosity and morphology, or the periodical distribution of metals that leads to their uniform dispersion in the derivatives, as well as the abundance of accessible active sites [21]. Among the challenges for the fabrication of MOF-derived metal/carbon hybrids, the main one is related to chemical bonding between metal sites and the carbon matrix, since this defines the structural stability and the electron transfer efficiency. Uncertainty about the bonding strength increases the risk of losing metal active sites during the catalyst usage and, additionally, the metal sites are vulnerable to deactivation because of shedding, oxidation, agglomeration or dissolution under the harsh oxidizing conditions of HEF [22]. The carbonaceous backbone may also undergo severe collapse due to hydraulic shock, making the material difficult to recover.

Core-shell catalysts, which consist of an active core embedded in a protective shell, are especially promising among pyrolyzed MOF derivatives [23,24]. In particular, porous shells are intended to retard the deactivation of the catalyst core by offering the inner active centers a tight protection, while simultaneously ensuring the diffusion of oxidants and pollutants from the bulk. Ideally, such confinement may result in reactant enrichment, presumably becoming an optimal strategy to boost reactivity [23,25]. The core–shell design has attracted great attention in the advanced oxidation processes (AOPs) field. Zhang et al. [26] fabricated a CoN/CN@SiO_2 nanoreactor to enhance the degradation of tetracycline in persulfate system. Pan et al [24] prepared a bifunctional $MnFe_2O_4$@HZO core–shell structure to activate persulfate for nitrilotrismethylenephosphonic acid removal. Nonetheless, these and other examples make in evidence that the core–shell catalysts may still be further improved, since the in many cases the shell acts as a barrier that limits the contact between reactants, thereby decelerating the degradation of contaminants. Therefore, precise regulation of the shell porosity and the thickness is mandatory in future catalyst design [23].

In this work, core–shell particles are synthesized to synergistically enhance the activity, stability and recyclability of MOF derivatives during the HEF treatment. In particular, the pyrolyzed derivative of a typical Fe-MOF like MIL-88B(Fe) was confined in mesoporous SiO_2 to form a core–shell structure (Fe/C@mSiO_2). Note that the high catalytic activity of MIL-88B(Fe) and its derivatives in H_2O_2/PMS-based AOPs has been attributed due to the abundant unsaturated iron active centers and fast Fe(II) recycling, although the excessive iron dissolution and low stability in water still impede their practical application [27–29]. In our work, nano-silica has been selected as the shell because of its three-dimensional flocculent mesh quasi-particle structure, which can enhance the strength and chemical resistance of the final catalysts [30]. The SiO_2 shell was thus employed as a multifunctional platform with different roles that have not been sufficiently explored for application in water treatment by HEF process. In particular, the shell is aimed at serving as a multichanneled porous barrier that protects the Fe/C core while enhancing the transport of H_2O_2 generated in situ and bisphenol A (BPA) used as target pollutant. In addition, it is expected to offer a confined microenvironment for the subsequent $^{\bullet}OH$ production and BPA degradation. Moreover, magnetic properties were conferred to the Fe/C core to favor the post-treatment recovery. The performance of the Fe/C@mSiO_2 was evaluated by comparing the effect of operation parameters on degradation efficiencies of BPA in different systems. The intrinsic mechanisms can be associated with mass transport and electron transfer enhancement, as has been deduced from the correlation with catalyst characterization, finite element analysis and radical scavenging experiments.

2. Materials and methods

2.1. Catalyst synthesis

The detailed synthesis route to obtain MIL-88B(Fe), MIL-88B(Fe)@mSiO_2 and Fe/C@mSiO_2 is schematized in Fig. 1a. First, mixed-valence MIL-88B(Fe) with increased amounts of Fe(II) centers and unsaturated metal sites was fabricated following an Fe(II) substitution method [31]. Typically, 1.62 g $FeCl_3{\cdot}6H_2O$, 0.80 g $FeCl_2{\cdot}4H_2O$ and 1.66 g terephthalic acid were dissolved into 50 mL N,N-dimethylformamide to form a homogeneous solution. Then, a few milliliters of 2 M NaOH solution were added dropwise under vigorous stirring. Subsequently, the as-obtained yellow mixture was transferred into a 100 mL Teflon-lined stainless steel autoclave and heated at 100 °C for 12 h. Once cooled down naturally, the resulting powder was collected by centrifugation and repeatedly rinsed with water and ethanol. The final MIL-88B(Fe) was dried overnight at 70 °C.

The MOF was coated with a SiO_2 shell via the classic Stöber method using cetyltrimethylammonium bromide (CTAB) as template [32]. First, 400 mg of MIL-88B(Fe) and 5 g of CTAB were uniformly dispersed into a 5:1 (v/v) water/ethanol mixture (total volume of 240 mL), which was then heated to 50 °C and, subsequently, 1 mL $NH_3{\cdot}H_2O$ solution was added to form solution A. In parallel, solution B was prepared by mixing 1 mL tetraethylorthosilicate (TEOS) and 7.5 mL cyclohexane (CYH), dispersed in a small volume of ethanol. Solution B was poured dropwise (5 times, almost 6 mL each, at 1 h interval to slow down the polymerization and hydrolysis rates of TEOS) into the solution A, followed by stirring for 6 h. The MIL-88B(Fe)@mSiO_2 was collected by centrifugation, washing several times with water and ethanol. The catalysts with different shell thickness were prepared following a similar procedure but employing different wt/v ratios of MIL-88B(Fe) and TEOS, whereas the pore channel dimensions of the catalyst shell were regulated by varying the TEOS/cyclohexane v/v ratio.

To obtain the Fe/C@mSiO_2, 120 mg MIL-88B(Fe)@mSiO_2 were transferred into a tube furnace and heated at 550 °C (or other

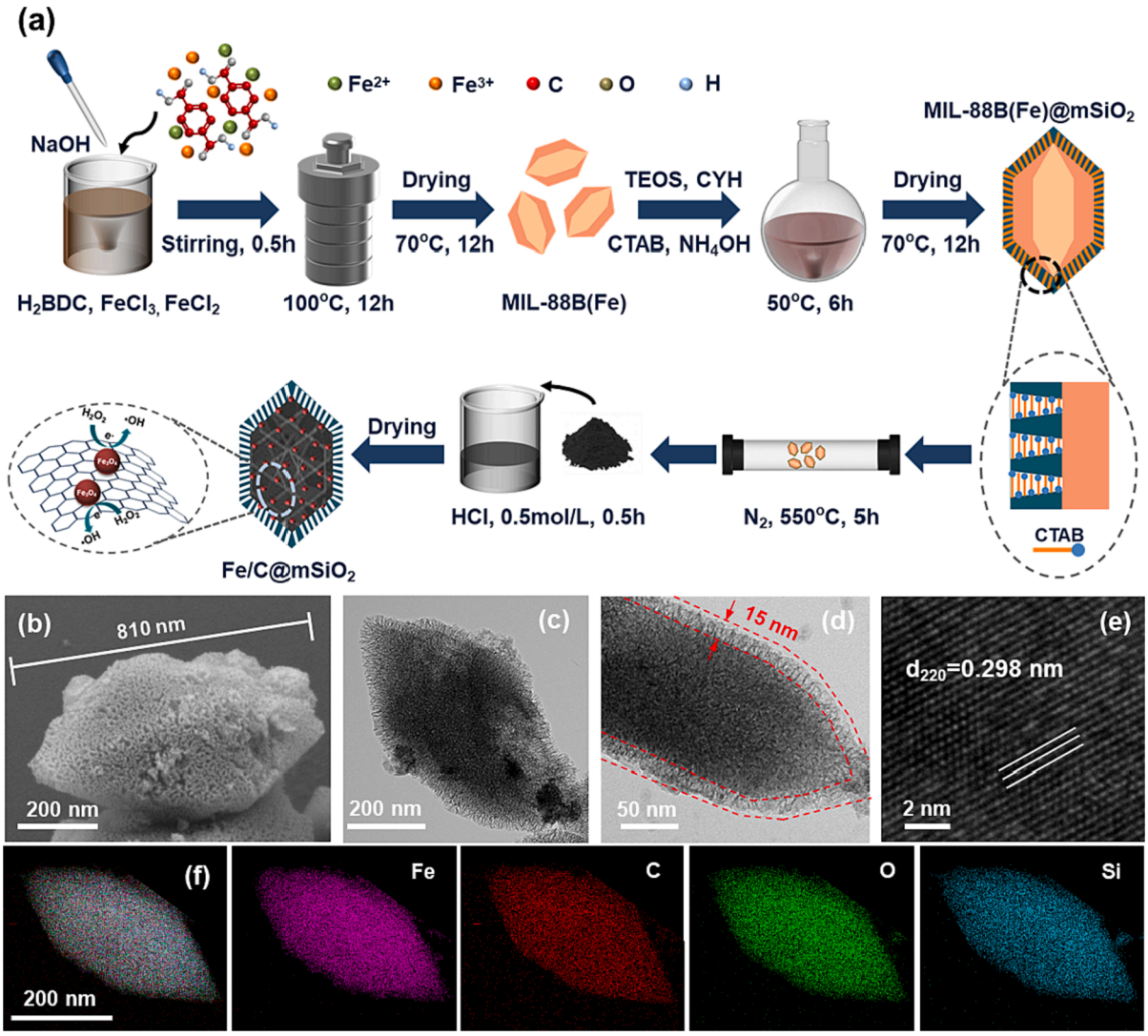

Fig. 1. (a) Schematic illustration of the synthetic route to obtain the Fe/C@mSiO$_2$, exemplifying the pyrolysis made at 550 °C. (b) SEM and (c-e) TEM images of Fe/C@mSiO$_2$ at different magnifications. (f) TEM elemental mapping of Fe, C, O and Si in Fe/C@mSiO$_2$.

temperatures) for 5 h under N_2 atmosphere. The carbonization product was treated with 0.5 M HCl solution for 0.5 h at 70 °C, then rinsed with water and dried overnight. The MIL-88B(Fe) derivatives without shell were prepared following an analogous pyrolysis procedure.

2.2. Evaluation of HEF performance

The electrolytic assays were carried out in a single chamber glass cell with 160 mL of solution kept at room temperature with a water bath. The cell was equipped with a 3 cm^2 gas-diffusion electrode as the cathode, with air flowing at 1 L min^{-1} for constant in-situ H_2O_2 production, and a 3 cm^2 Ti|IrO_2-based dimensionally stable anode (DSA) plate or a 3 cm^2 boron-doped diamond thin film (BDD) anode. The gap between the electrodes was around 1.0 cm [33]. Constant current was applied using a DC power supply (IT6302 from ITECH, China). The HEF trials were started after catalyst addition. Samples were filtered with 0.22 μm PTFE syringe filters to remove particles.

2.3. Characterization and analytical procedures

The morphology and elements distribution in the catalysts were assessed by scanning electron microscopy (SEM) and high-resolution transmission electron microscopy (HRTEM) coupled to energy-dispersive X-ray spectrometry (EDS). The X-ray diffraction (XRD) was employed to analyze the crystallite structure, using a Bruker D8 Advance with Cu $K_{\alpha1}$ radiation ($\lambda = 1.5406$ Å) from 5° to 90° at a scanning rate of 5 degree min^{-1}. X-ray photoelectron spectroscopy (XPS) served to investigate the chemical and electronic structures of the catalysts, using a ThermoScientific K-Alpha with Al K_α radiation in steps of 0.1 eV, calibrated internally using the C 1s (E_b = 284.6 eV). Raman analysis, carried out to identify the graphitization degree, was made with a Raman microscope (Horiba LabRAM HR Evolution, Japan). The specific surface area (S_{BET}) and pore volume were investigated using a surface area analyzer (Micromeritics ASAP-2460,USA). The Fourier transform infrared (FTIR) spectra were collected on a TermoScientific Nicolet iS20 spectrometer. The magnetic properties were analyzed on a LakeShore 7404 susceptometer. Electrochemical impedance spectroscopy (EIS), Tafel polarization and chronoamperometry were carried out on a CHI 760E electrochemical workstation.

The analytical methods for the measurement of pH, dissolved iron and H_2O_2 concentrations, and total organic carbon (TOC) content are presented in Text S1 in Supplementary Material (SM). The degradation performance was evaluated by determining the concentration of organic pollutants using reversed-phase high performance liquid chromatography (HPLC, SCION6000, China), as described in Text S2 in SM. The finite element analysis was carried out with COMSOL Multiphysics 5.1

software using the dimensions measured from TEM images. The setup and conditions employed for the electrochemical characterization are summarized in Text S3 in SM.

3. Results and discussion

3.1. Structural characterization of the catalysts

The SEM and TEM images shown in Fig. 1b–e reveal the morphology and microstructure of the as-obtained Fe/C@mSiO$_2$ powder. A rod-like shape with a major length of around 810 nm can be observed in Fig. 1b, which was clearly inherited from its MIL-88B(Fe) precursor (Fig. S1). The TEM images in Fig. 1c and d show the encapsulation achieved in the pyrolyzed MIL-88B(Fe) derivative, exhibiting a 15 nm-thick SiO$_2$ shell. The ordered mesoporous channels in the SiO$_2$ layer are clearly identified, which are expected to provide favorable routes for the delivery of the pollutant and H_2O_2 molecules. The formation of mesoporous channels can be attributed to the addition of the porogen CTAB during the synthesis [34,35]. The HRTEM image of Fe/C@mSiO$_2$ (Fig. 1e) clearly displays the lattice fringes with interplanar distance of 0.298 nm, corresponding to the lattice spacing of the (220) plane of Fe_3O_4 [36–38]. Moreover, the EDS mapping in Fig. 1f allows concluding that the Fe/C@mSiO$_2$ contained C, O, Si, and Fe elements, and the iron sites were uniformly dispersed in the inner core without distinct agglomeration. In turn, the SiO$_2$ shell was quite uniform as well. Note that the carbonization of MIL-88B(Fe) to achieve carbon-supported $Fe_2O_3/Fe_3O_4/Fe^0$ particles usually entails severe aggregation of iron sites, resulting in the formation of relatively large nanoparticles. This is detrimental because only the surface iron active sites can be involved in the catalytic reactions [39–41]. The successful synthesis of the core–shell nanoreactors is thus expected to not only improve the stability of the catalyst core, but also boost the transformation of pollutants and H_2O_2 into the core.

The XRD patterns of MIL-88B(Fe) and its derivatives are shown in Fig. 2a. As can be seen, the main diffraction peaks of MIL-88B(Fe) appear at 9.2° (002), 12.4° (102), 16.6° (110), 19.2° (200) and 21.8° (202), which match well with the simulated diffractogram reported in the CIF database, corroborating the successful synthesis of MIL-88B(Fe) [10,42]. The main peaks in the pattern of pyrolyzed MIL-

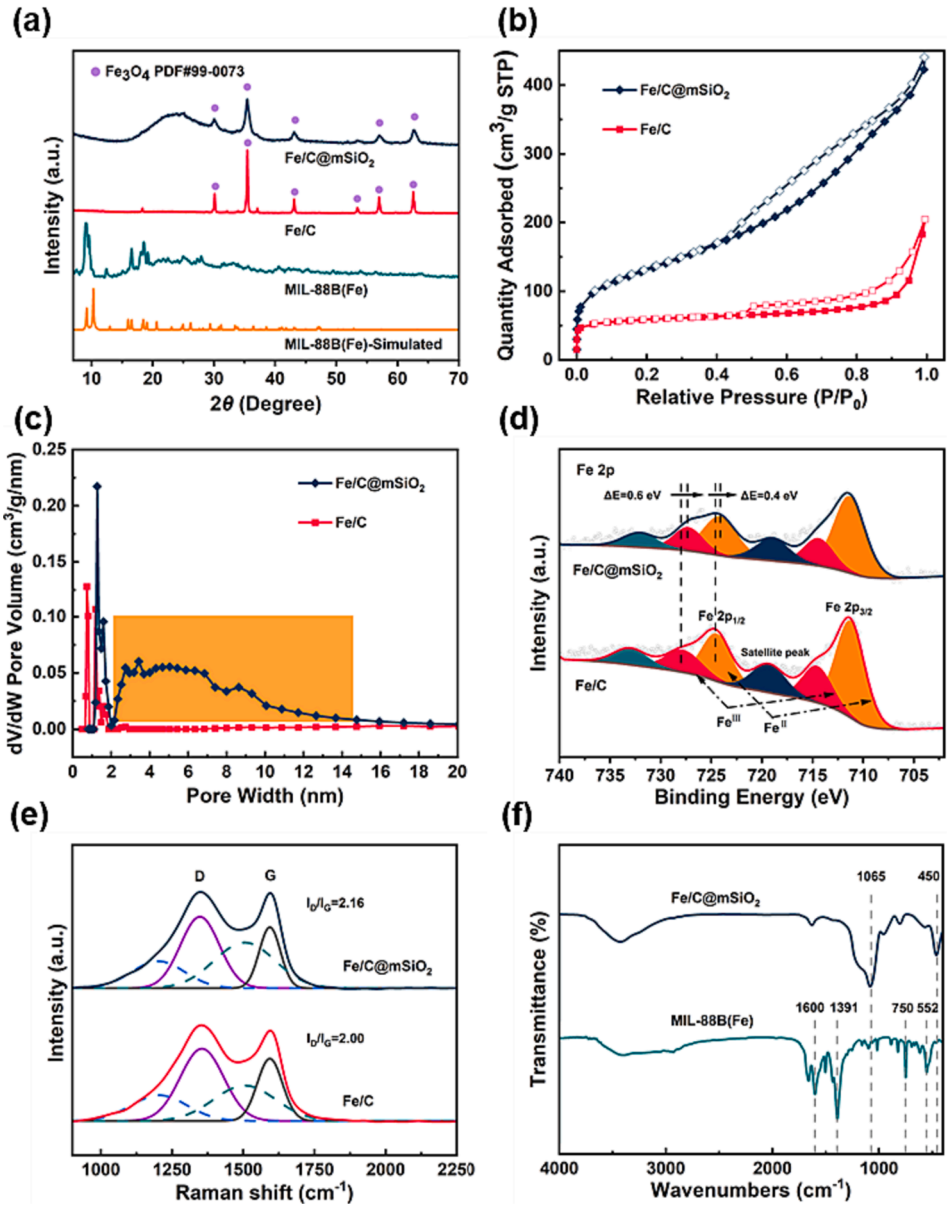

Fig. 2. (a) XRD patterns of MIL-88B(Fe) (simulated and synthesized), Fe/C and Fe/C@mSiO$_2$. (b) N_2 adsorption–desorption isotherms. (c) Pore size distribution curves. (d) Fe 2p XPS spectra and (e) Raman spectra of Fe/C and Fe/C@mSiO$_2$. (f) FTIR spectra of MIL-88B(Fe) and Fe/C@mSiO$_2$. MOF pyrolysis made at 550 °C.

88B (i.e., Fe/C) are found at 30.0°, 35.4°, 43.1°, 56.9°, and 62.5°, which can be ascribed to (220), (311), (400), (511) and (440) crystal planes of Fe_3O_4 (PDF#99–0073) [43,44]. Additionally, a week broad peak is observed at around 20°-30° in the pattern of Fe/C@$mSiO_2$, which can be assigned to amorphous SiO_2 [45,46]. The other diffraction peaks in the latter catalyst are quite similar to those of Fe/C, suggesting that Fe_3O_4 is the predominant structure of the core. The peak intensities of Fe/C@$mSiO_2$ are lower due to the presence of the $mSiO_2$ shell, which slightly blocks the penetration of X-rays through the particles [32,47,48]. From these results, it can be stated that the coating with the SiO_2 shell did not alter the crystallinity and purity of the pyrolyzed MIL-88B (Fe) derivative.

The N_2 adsorption–desorption isotherms of Fe/C and Fe/C@$mSiO_2$ are shown in Fig. 2b. Type IV isotherms with typical hysteresis loops at $P/P_0 > 0.4$ are observed for both samples, suggesting the presence of mesopores. In addition, the desorption branch at $P/P_0 = 0.4–0.5$ was greatly affected due to the delayed evaporation of N_2 from the Fe/C@$mSiO_2$, being blocked by the SiO_2 shell [32,49]. As evidenced in Fig. 2c, both pyrolyzed derivatives present small mesopores with diameter range of 1.2–1.7 nm, which are inherited from the MIL-88B (Fe) precursor [50,51]. Meanwhile, the Fe/C@$mSiO_2$ shows extra larger mesopores with broad pore sizes in the range of 2.5–14.8 nm, which are introduced by the SiO_2 shell. The larger pore size and wider pore size distribution range of Fe/C@$mSiO_2$ can facilitate the mass transport during the catalytic reactions. Additionally, the double-layer surface of the core–shell structure endows Fe/C@$mSiO_2$ a high BET specific surface area of 514.1 $m^2\ g^{-1}$ and high pore volume of 0.73 $cm^3\ g^{-1}$, as compared to the values obtained for Fe/C (216.0 $m^2\ g^{-1}$ and 0.22 $cm^3\ g^{-1}$). This seems interesting to provide the reactants with greater access to the inner active sites.

The XPS analysis contributed to understand the chemical composition and electronic structure of the two materials obtained by pyrolysis at 550 °C. The survey spectra of the Fe/C and Fe/C@$mSiO_2$ catalysts shown in Fig. S2a reveal the presence of Fe, O and C elements, with Si also appearing in the latter, serving to verify the successful coating with SiO_2 as discussed from TEM analysis. The Si 2p peak at 104.0 eV arises from the Si^{4+} in the SiO_2 shell (Fig. S2b). The high-resolution Fe 2p spectrum of Fe/C in Fig. 2d consists of two sets of spin orbital peaks (Fe $2p_{3/2}$ and Fe $2p_{1/2}$). The peaks with the binding energies centered at 714.7 and 728.0 eV can be associated to Fe(III) species, whereas the peaks at 711.4 and 724.6 eV are attributed to Fe(II) species. Moreover, the two broad peaks at 719.5 and 733.3 eV are ascribed to the satellite peaks of Fe 2p. The high proportion of Fe(II) species in the pyrolyzed products was due to the successful incorporation of Fe(II) in the oxo-node of MIL-88B (Fe) precursor, which will certainly boost the activity of the catalyst during HEF process (see below) [31]. On the other hand, the binding energies of both Fe(III) and Fe(II) in Fe/C@$mSiO_2$ are negatively shifted by around 0.6 and 0.4 eV, which can be attributed to the electronic metal-support interaction between Fe and SiO_2, leading to the decrease in the electron density of Fe [19,52]. Worth noting, the proportion of Fe(II) species remained almost unaltered, demonstrating that the introduction of the SiO_2 shell scarcely affects the inner core structure. Finally, the C 1s spectra of Fe/C and Fe/C@$mSiO_2$ can be deconvoluted into three peaks centered at 284.8, 286.4 and 288.8 eV, which are assigned to C-C, C-O-C and C=O functional groups (Fig. S2c) [53].

The defect states of the carbon component in the Fe/C@$mSiO_2$ and Fe/C catalysts were further analyzed by Raman spectroscopy (Fig. 2e). The defective D and graphitic G bands are observed at 1350 cm^{-1} and 1600 cm^{-1}, respectively, indicating the presence of carbonaceous content that derives from the MOFs ligands [6]. The intensity ratio of the D to G band accounts for the defective degree of the carbon. The I_D/I_G values of Fe/C and Fe/C@$mSiO_2$ were 2.00 and 2.16, respectively, suggesting that the introduction of SiO_2 shell enhances the degree of carbon defectiveness. As reported, abundant defects can accelerate the adsorption of pollutants and enhance the electron transfer during the electrochemical reactions [54].

Moreover, the FITR spectra of MIL-88B(Fe) and Fe/C@$mSiO_2$ are shown in Fig. 2f. For MIL-88B (Fe), the peaks at 1600 cm^{-1} and 1391 cm^{-1} can be attributed to the antisymmetric and symmetric stretching vibrations of –COOH groups, respectively. The peak at 750 cm^{-1} has been indexed to the C–H bending vibrations of benzene ring, whereas the peak at 552 cm^{-1} is assigned to the Fe-O bond stretching [55]. These results demonstrate again the successful synthesis of MIL-88B(Fe). Noticeably, all peaks disappeared in the spectrum of Fe/C@$mSiO_2$, which was accompanied by the appearance of two intense peaks at 450 cm^{-1} and 1065 cm^{-1} attributed to the Si-O-Si bonds. This means that the organic ligands in the precursor were fully carbonized during the thermal treatment and SiO_2 shell was formed concomitantly [32].

The magnetism of Fe/C@$mSiO_2$ was also investigated. As shown in Fig. S2d, the saturation magnetization value was around 9.3 emu g^{-1}, a sufficiently strong magnetic property to allow the efficient recovery of the catalyst in the presence of an external magnetic field (i.e., magnet).

3.2. Catalytic performance and stability

To assess the catalytic activity and stability of Fe/C@$mSiO_2$, the degradation of BPA by different processes was comparatively studied. Prior to deepen into the electrochemical trials, the adsorption of BPA on Fe/C and Fe/C@$mSiO_2$ was evaluated. As shown in Fig. S3, the presence of 0.2 g L^{-1} Fe/C only yielded a negligible BPA removal of 4.7 %, whereas the Fe/C@$mSiO_2$ had a larger adsorption capacity, attaining 38.2 % BPA removal. This can simply accounted for by the larger surface area of the latter (514.1 $m^2\ g^{-1}$), with the mesoporous SiO_2 nano-shells providing abundant permeable channels for the mass transport of BPA [56]. Moreover, the electrostatic attraction between BPA and Fe/C@$mSiO_2$ was also stronger thanks to the shell material, contributing to the better adsorption performance (details can be seen in Section 3.3).

The electrochemical oxidation with the IrO_2-based DSA as the anode allowed attaining a small BPA removal of 17.5 % after 120 min of electrolysis (Fig. 3a), as a result of the mild oxidation by $IrO_2(^{\bullet}OH)$ produced anodically via reaction (4) [57]. In contrast, the MIL-88B(Fe)-catalyzed HEF process led to complete removal of BPA at 120 min, implying a strong catalytic ability of the uncoated material; however, the iron leaching was as high as 5.40 mg L^{-1} at the end of the trial (Fig. 3b). Despite the fact that mixed-valence MIL-88B(Fe) exhibits a high amount of Fe(II) centers that can be used for Fenton's reaction, its stability in water is rather low. Accordingly, the dissolved Fe^{2+} species can trigger homogeneous Fenton's reaction to produce $^{\bullet}OH$, thus competing with the presumed heterogeneous BPA degradation. When the same catalyst was pyrolyzed, yielding the Fe/C catalyst, the HEF treatment could only reach 41.3 % BPA decay at 120 min. The corresponding low iron leaching of 0.57 mg L^{-1} (Fig. 3b) prevented the significant occurrence of homogeneous Fenton's reaction and hence, $^{\bullet}OH$ essentially resulted from the heterogeneous route. The unsatisfactory performance was due to the limited mass transport of the reactants and quick diffusion and quenching of $^{\bullet}OH$. The MIL-88B(Fe)@$mSiO_2$-catalyzed HEF process resulted in a similar BPA removal (38.7 %), which means that the introduction of a protective $mSiO_2$ shell significantly slowed down the decomposition of labile mixed-valence MIL-88B(Fe). This is confirmed by the low iron leaching (1.17 mg L^{-1}). Considered as a whole, all these results demonstrate that the iron active sites in MIL-88B (Fe) are very accessible, but this characteristic is insufficient to maintain the effective production of $^{\bullet}OH$ because of the gradual destruction of the catalyst (with Fe^{2+} leaching). Conversely, the Fe/C@$mSiO_2$-catalyzed HEF process exhibited an outstanding performance as compared to all the other trials, reaching the complete BPA removal with extremely low iron leaching (0.11 mg L^{-1}). The degradation of BPA during the different electrochemical trials agrees perfectly with a pseudo-first-order kinetics. As depicted in Fig. 3c, the use of Fe/C@$mSiO_2$ led to the highest rate constant (0.035 min^{-1}), being 1.5-fold greater than that achieved with MIL-88B(Fe) and about 9-fold greater than those of Fe/C- and MIL-88B

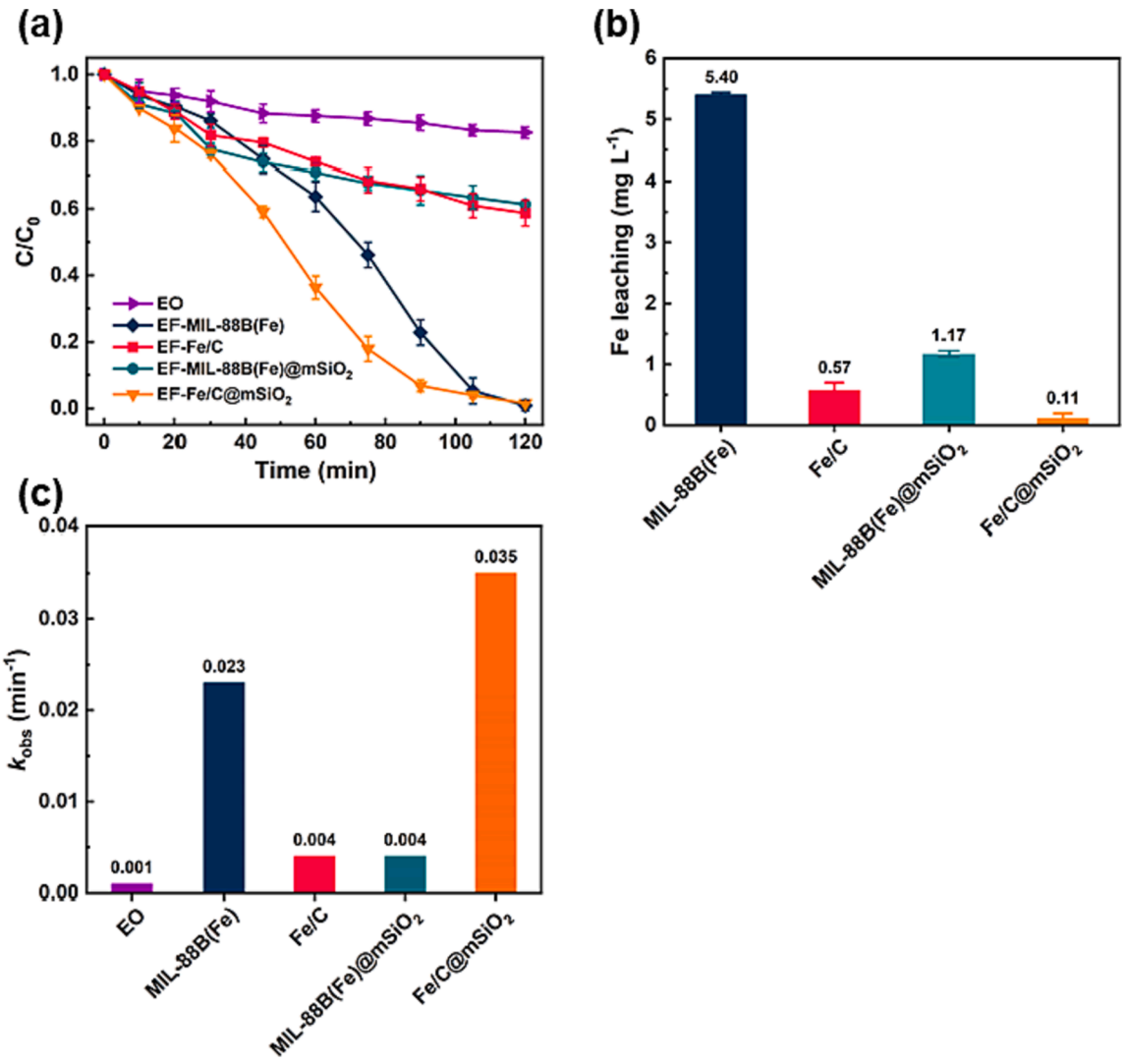

Fig. 3. (a) Normalized BPA concentration decay during different treatments of 160 mL of 0.11 mM BPA solutions. Comparison of (b) leached iron concentrations after 120 min and (c) pseudo-first-order rate constants determine from the trials shown in plot (a). General conditions: [Catalyst] = 0.2 g L^{-1}; current = 100 mA; initial pH = 6.2; IrO_2-based anode; MOF pyrolysis made at 550 °C.

(Fe)@mSiO$_2$-catalyzed HEF. In conclusion, the mesoporous SiO_2 shell confers a confined microenvironment that allows boosting the water stability and the catalytic activity.

The catalytic properties of Fe/C@mSiO$_2$ highly depends on the pyrolysis temperature. Fig. 4a illustrates the BPA degradation curves for the HEF treatment with different catalysts fabricated at the temperatures ranging from 300 °C to 900 °C. A partial BPA removal as high as 90.4 % was achieved at 120 min by Fe/C@mSiO$_2$-300 catalyzed HEF process but, unfortunately, the iron leaching was very high (1.49 mg L^{-1}), meaning that the BPA degradation counted on a significant contribution of the homogeneous Fenton's reaction (Fig. S4a). Furthermore, as shown by the XRD patterns in Fig. 4b, the low calcination temperature of 300 °C only led to partial conversion of Fe nodes of MIL-88B(Fe), yielding Fe_2O_3. The incomplete collapse of the raw Fe-MOF reduced its structure stability, failing to form abundant accessible Fe(II) active centers due to the limited Fe(III) reduction efficiency [58]. Fig. 4a informs about the superior catalytic performance of Fe/C@mSiO$_2$-550. The higher carbonization temperature ensured the efficient decomposition of the organic framework in MIL-88B(Fe) to produce homogeneous carbon substrate, and the release of pyrolysis gas favored the generation of a porous structure. The iron sites were effectively converted into ultrasmall Fe_3O_4 crystals, which were uniformly dispersed on the carbonaceous matrix. Such unique structure endowed the Fe/C@mSiO$_2$-550 with high specific surface area and multiple accessible active sites. In contrast, further increase of the pyrolysis temperature to 800 °C and 900 °C was detrimental, evidenced from the inhibited abatement of BPA (Fig. 4a). Much higher temperature could further convert the Fe_3O_4 into Fe_2SiO_4 (Fig. 4b), leading to the collapse of the core–shell structure and the loss of active sites. Moreover, the carbon skeleton shrinks dramatically at extremely high temperature, leading to the reduction in the porosity and the aggregation of the iron nanoparticles [59]. Therefore, 550 °C was considered as the optimal pyrolysis temperature to fabricate the Fe/C@mSiO$_2$.

The amount of TEOS during the synthesis is critical to the SiO_2 thickness, which might affect the catalytic performance. The BPA decays using Fe/C@mSiO$_2$ catalysts produced at different MIL-88B(Fe)/TEOS w/v ratio are depicted in Fig. S4b. The increase in the ratio from 200:1 to 400:1 resulted in a substantial acceleration of the BPA degradation, rising from 80.9 % to total removal at 120 min. Nonetheless, when further increasing the ratio to 500:1, the removal efficiency dropped to 71.3 % at 120 min. The shell thickness is expected to increase as the MIL-88B(Fe)/TEOS ratio is diminished [60]. The mesoporous SiO_2 shells provide abundant channels for the mass transport of BPA and H_2O_2 but, if the transport channels become too long, the reactants and/

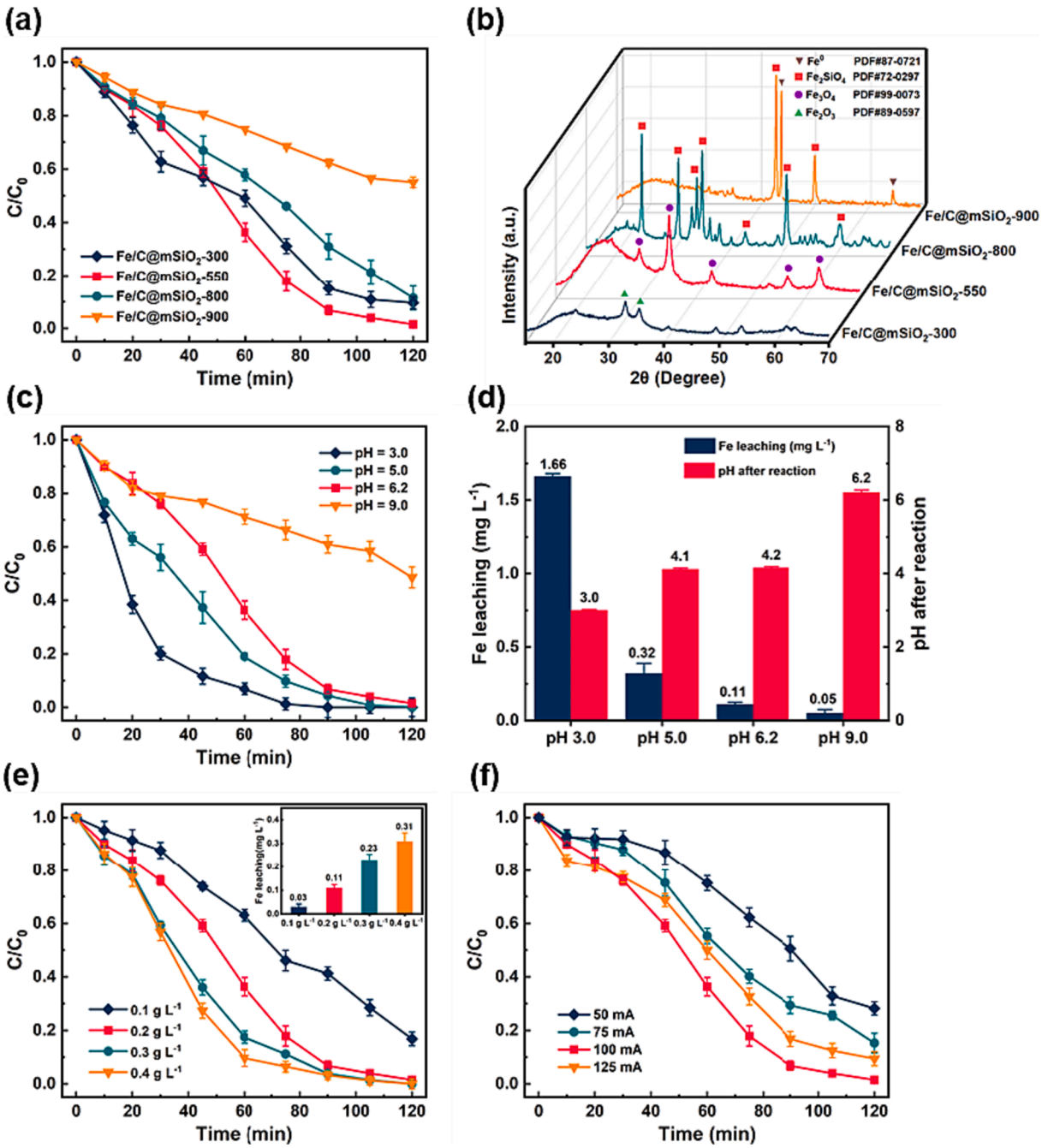

Fig. 4. (a) Effect of synthesis temperature on the performance of Fe/C@mSiO$_2$-catalyzed HEF process and (b) XRD patterns for each catalyst in plot (a). Effect of (c) initial pH, (e) catalyst dosage and (f) applied current on BPA decay in the Fe/C@mSiO$_2$-catalyzed HEF system. (d) Leached iron concentration and final pH after 120 min of the trials shown in plot (c). The inset in plot (e) shows the leached iron concentrations after 120 min of the trials depicted in the main plot. General conditions, except when a specific parameter is modified: [BPA] = 0.11 mM; [catalyst] = 0.2 g/L; current = 100 mA; initial pH = 6.2; IrO$_2$-based anode; MOF pyrolysis made at 550 °C.

or pollutants can be trapped and are not able to access the core of the catalyst. Furthermore, the agglomeration of iron active sites may occur at too high relative TEOS content [61]. At excessively low TEOS amount (i.e., highest MIL-88B(Fe)/TEOS ratio of 500:1), the specific surface area and porosity of the catalyst largely decrease, causing a poor mass transport. On the other hand, the iron leaching decayed upon increase of TEOS content (Fig. S4c), suggesting that the core coated with thicker SiO$_2$ shell is more protected.

The addition of cyclohexane oil phase during the synthesis can greatly affect the assembly of the SiO$_2$ shell, as it swells the shell templates by occupying the hydrophobic cavity, eventually leading to the increase in the mesopore size [62]. Herein, different cyclohexane/TEOS v/v ratios were examined (at fixed TEOS volume) for the fabrication of Fe/C@mSiO$_2$, and the corresponding catalytic performance is shown in Fig. S4d. When increasing the cyclohexane/TEOS ratio from 2.5:1 to 7.5:1, the BPA removal increased from 75.2 % to 100 %, whereas a further increase in the ratio to 10.0:1 was detrimental. A high amount of cyclohexane that transfers into the cavity of the SiO$_2$ shell can expand the mesopores, providing more channels for the mass transport. However, excessive cyclohexane can form large droplets, which are temporarily unstable for efficient interfacial co-assembly [35]. Besides, the iron leaching increased from 0.01 mg L^{-1} to 0.20 mg L^{-1} with the increase

in the cyclohexane/TEOS ratio from 2.5 to 10.0, demonstrating that the expansion of the mesopore size affects the catalyst stability (Fig. S4e).

The effect of various operation factors, including initial pH, catalyst dosage and applied current, on the BPA degradation by Fe/C@mSiO$_2$-catalyzed HEF process was investigated. As shown in Fig. 4c, the quickest BPA decay was observed at initial pH 3.0, achieving the total removal at 75 min. Such enhanced performance can be attributed to the greater oxidation potential of $^{\bullet}$OH at acidic pH and, more important, the contribution of homogeneous Fenton's reaction initiated by the dissolved iron ions (1.66 mg L^{-1}, Fig. 4d) [5]. As a very remarkable feature, overall BPA removal could still be achieved at initial pH 5.0 and 6.2, with extremely low iron leaching of 0.32 and 0.11 mg L^{-1}, respectively, demonstrating the excellent catalytic activity and stability of the catalyst at near-neutral pH. Further increase of initial pH to 9.0 caused a drastic deceleration of BPA removal, only attaining 51.4 % due to the low oxidation ability of $^{\bullet}$OH and the accelerated self-decomposition of H_2O_2 at alkaline pH [10]. Note that the solution pH tended to diminish (Fig. 4d), which can be explained by the production of acidic intermediates like carboxylates [63].

Fig. 4e illustrates that the increase in the catalyst dosage from 0.1 to 0.3 g L^{-1} gave rise to a substantial enhancement of the BPA decay, with a significant increase in the degradation rate constant from 0.014 to 0.040 min^{-1} at the expense of only a small rise in iron leaching from 0.03 to 0.23 mg L^{-1} (see inset). The gradually greater catalytic performance is therefore due to the higher amount of available active sites, rather than the occurrence of homogeneous EF. The enhancement of BPA degradation was insignificant when increasing the dosage to 0.4 g L^{-1}, which can be ascribed to the parasitic reaction between the excessive iron sites and $^{\bullet}$OH [6]. Finally, as deduced from Fig. 4f, the increase in the applied current had a positive effect on the BPA removal. The higher current was associated to a greater H_2O_2 production (Fig. S4f), with the consequent promotion of Fenton's reaction to generate more $^{\bullet}$OH.

The TOC abatement during the Fe/C@mSiO$_2$-catalyzed HEF treatment was assessed as well. Fig. S5 highlights a substantial TOC abatement of 62.0 % after 480 min of electrolysis using the IrO$_2$-based DSA anode at 100 mA. The mineralization was significantly increased to 90.0 % when replacing the anode with BDD, which can be well explained by the synergistic action of the $^{\bullet}$OH formed in the core of the catalyst and the physisorbed BDD($^{\bullet}$OH) produced at the anode surface. As reported, the oxidation ability of BDD($^{\bullet}$OH) is clearly superior to that of IrO$_2$($^{\bullet}$OH) [64]. The study of the performance of the Fe/C@mSiO$_2$-catalyzed HEF system was further extended by degrading different organic pollutants in their single solutions. As depicted in Fig. 5a, the complete removal of BPA and amoxicillin, 97.0 % removal of tetracycline hydrochloride and 91.6 % removal of naproxen could be achieved at 120 min, whereas lower removal efficiencies around 75 % were obtained for diclofenac sodium, carbamazepine and 2,4-dichlorophenol. The relatively good performance regarding the degradation of most organics was due to the nonselective nature of $^{\bullet}$OH-mediated oxidation. Nonetheless, the physicochemical properties of the target pollutants, such as electron affinity and specific functional groups, can greatly affect their adsorption and reactivity with $^{\bullet}$OH, leading to different degradation efficiencies. Finally, the recyclability of Fe/C@mSiO$_2$ was assessed by performing consecutive trials with the used catalyst. The powder was always recovered by simple magnetic separation, followed by simple cleaning with ethanol and ultrapure water. As shown in Fig. 5b, the BPA removal efficiency still remained above 90 % in the 5th cycle, demonstrating the excellent recyclability of the protected catalyst. The slight deceleration

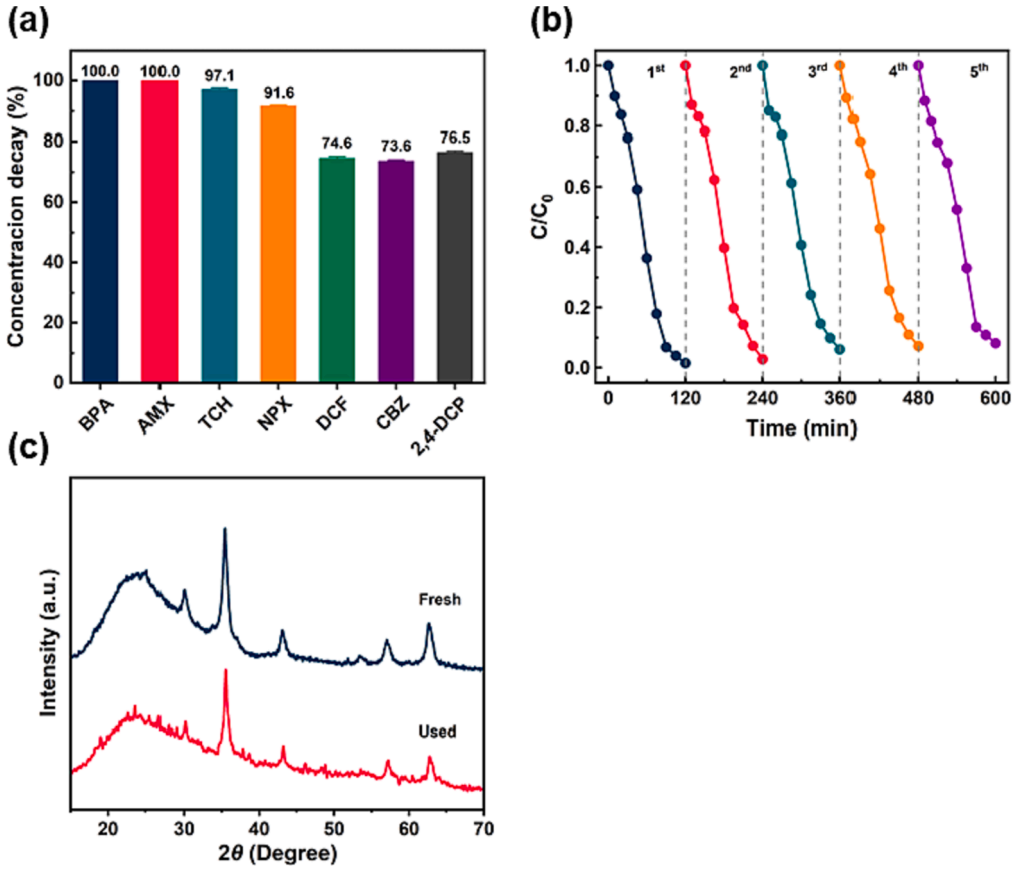

Fig. 5. (a) Performance of the Fe/C@mSiO$_2$-catalyzed HEF process considering different target organic pollutants: BPA, amoxicillin (AMX), tetracycline hydrochloride (TCH), naproxen (NPX), diclofenac sodium (DCF), carbamazepine (CBZ) and 2,4-dichlorophenol (2,4-DCP). General conditions: [Pollutant] = 10 mg C L^{-1}; [Catalyst] = 0.2 g L^{-1}; initial pH = 6.2; current = 100 mA; 120 min of electrolysis. (b) Recyclability test using the Fe/C@mSiO$_2$ in five consecutive HEF assays to treat BPA solutions under the conditions described in Fig. 3a. (c) XRD patterns of the fresh and used Fe/C@mSiO$_2$ catalyst. In all cases, MOF pyrolysis made at 550 °C.

in the degradation kinetics might be due to the passivation and deactivation of the core iron active sites and the possible blockage of the mesoporous channels in the SiO_2 shell. The used catalyst was further characterized by XRD analysis (Fig. 5c), revealing that the peak positions and intensities were not substantially altered upon usage. Therefore, the chemical structure and crystallinity remained very stable during the treatment. In conclusion, Fe/C@mSiO_2 exhibited great catalytic activity, stability and recyclability, being highly convenient for HEF process.

3.3. Mechanistic insights

In order to verify the confinement effect of the SiO_2-shelled nanoreactors, finite element analysis was carried out to simulate the concentration gradient distribution of BPA and $^{\bullet}OH$ along the Fe/C and Fe/C@mSiO_2 nanoparticles. As shown in Fig. 6a, when Fe/C particles were employed, BPA was mainly localized in the solution, with a small amount confined in/on the catalyst. In strong contrast, Fig. 6b shows that a large number of BPA molecules were trapped and accumulated into the porous channels of the SiO_2 shell and the core catalyst, demonstrating the nanoconfinement effect resulting from the use of core–shell nanoreactors [65]. The enhanced mass transport can be attributed to the better adsorption ability of Fe/C@mSiO_2 and the limited desorption of BPA due to the presence of vast nanoscale pores in the SiO_2 shell. The superior adsorption ability of the shelled catalyst was further confirmed by determining the zeta potential as a function of solution pH. As depicted in Fig. S6, the zeta potential of both Fe/C and Fe/C@mSiO_2 decreased with the increase in the pH value. The surface of Fe/C was positively charged at pH 6.2, whereas the surface of Fe/C@mSiO_2 was negatively charged. As reported elsewhere [66], BPA is positively charged since it predominates in the acidic form at pH 6.2, which means that the electrostatic attraction between BPA and Fe/C@mSiO_2 was favored. Also, the concentration distribution of $^{\bullet}OH$ along the two types of particles is depicted Fig. 6c and d. The generation of $^{\bullet}OH$ is expected to occur upon the reactive event between H_2O_2 and the active sites of the catalyst. However, a high amount of $^{\bullet}OH$ diffuses away from the Fe/C particle into the bulk, owing to the relatively high diffusion coefficient of this radical [67,68]. In contrast, the diffusion of $^{\bullet}OH$ is largely restricted in the case of Fe/C@mSiO_2 due to the confinement effect of the nanopores of the SiO_2 shell, resulting in a much higher steady-state concentration of $^{\bullet}OH$ inside the catalyst. Note that the $^{\bullet}OH$ generated from the heterogeneous Fenton's reaction usually attenuates rapidly during the diffusion from catalyst to solution because of its extremely short half-life (2×10^{-8} s), which significantly reduces the collision probability between pollutant molecules and $^{\bullet}OH$ [66]. The high $^{\bullet}OH$ concentration regions formed in the Fe/C@mSiO_2 greatly boost the collision probability between BPA and $^{\bullet}OH$, minimizing their waste in parasitic reactions.

Two types of $^{\bullet}OH$ can contribute to BPA degradation: free $^{\bullet}OH$ (i.e., $^{\bullet}OH_{free}$) available in the bulk (i.e., outside the core–shell nanoreactors), and surface-bound $^{\bullet}OH$ (i.e., $^{\bullet}OH_{ads}$) formed at the surface of catalyst. The role of these radicals was elucidated by means of radical scavenging experiments. As reported, *n*-butanol can efficiently scavenge both $^{\bullet}OH_{free}$ and $^{\bullet}OH_{ads}$, whereas KI can only eliminate $^{\bullet}OH_{ads}$ [57,69]. As shown in Fig. 7a, the BPA removal efficiency decreased to 55.0 % and 42.5 % in the presence of excess KI and *n*-butanol, respectively, demonstrating that the major contribution to BPA degradation corresponds to $^{\bullet}OH_{ads}$ in the Fe/C@mSiO_2-catalyzed HEF process. Conversely, the BPA removal was significantly inhibited in the presence of excess *n*-butanol during Fe/C-catalyzed HEF process, being barely affected by the addition of KI (Fig. 7b). From this, it can be interpreted that $^{\bullet}OH_{free}$ may play a considerable role in BPA degradation when using the non-confined catalyst, in agreement with the greater metal leaching that promotes homogeneous EF. These results are in good agreement with the observations in Fig. 6c and d, since the as-formed $^{\bullet}OH$ with Fe/C@mSiO_2 could be well confined in the core due to the nanoconfinement effect, while most of $^{\bullet}OH$ produced at Fe/C particles is free to diffuse into the bulk solution.

The EIS and Tafel tests were performed to evaluate the electron transfer during the catalytic processes. The Nyquist plots of Fe/C@mSiO_2 and Fe/C with the equivalent circuit displayed inside are shown in Fig. 7c. The interfacial charge transfer resistance (R_{ct}) was obtained from the fitting of the corresponding equivalent circuit, which informed about the ability of the catalyst to promote the internal

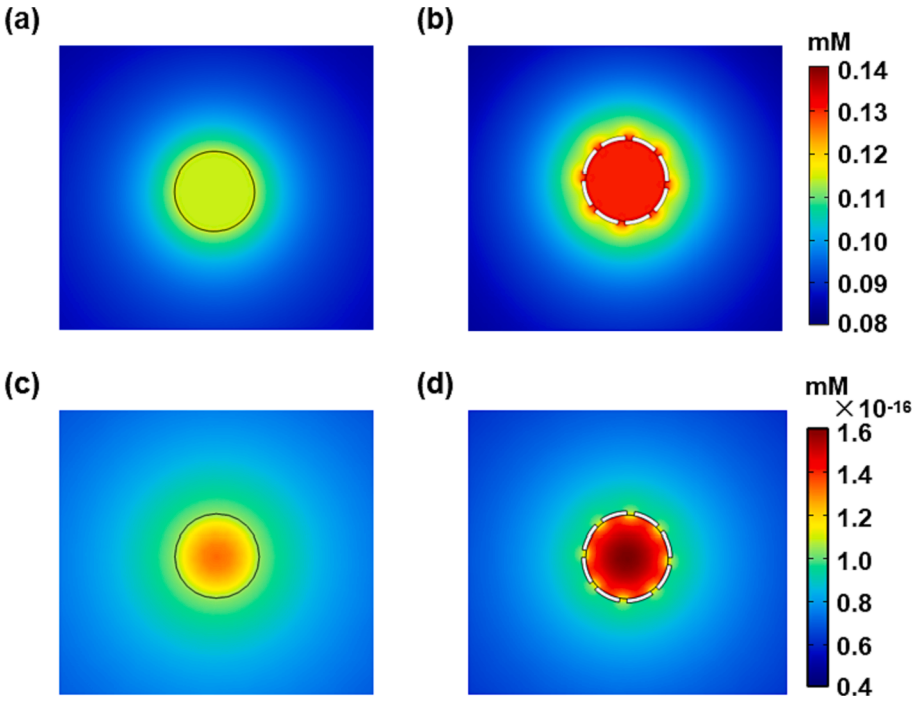

Fig. 6. Finite element analysis of simulated concentration gradient distribution of: (a, b) BPA and (c, d) •OH, employing (a, c) Fe/C and (b, d) Fe/C@mSiO_2, respectively. In all cases, MOF pyrolysis made at 550 °C.

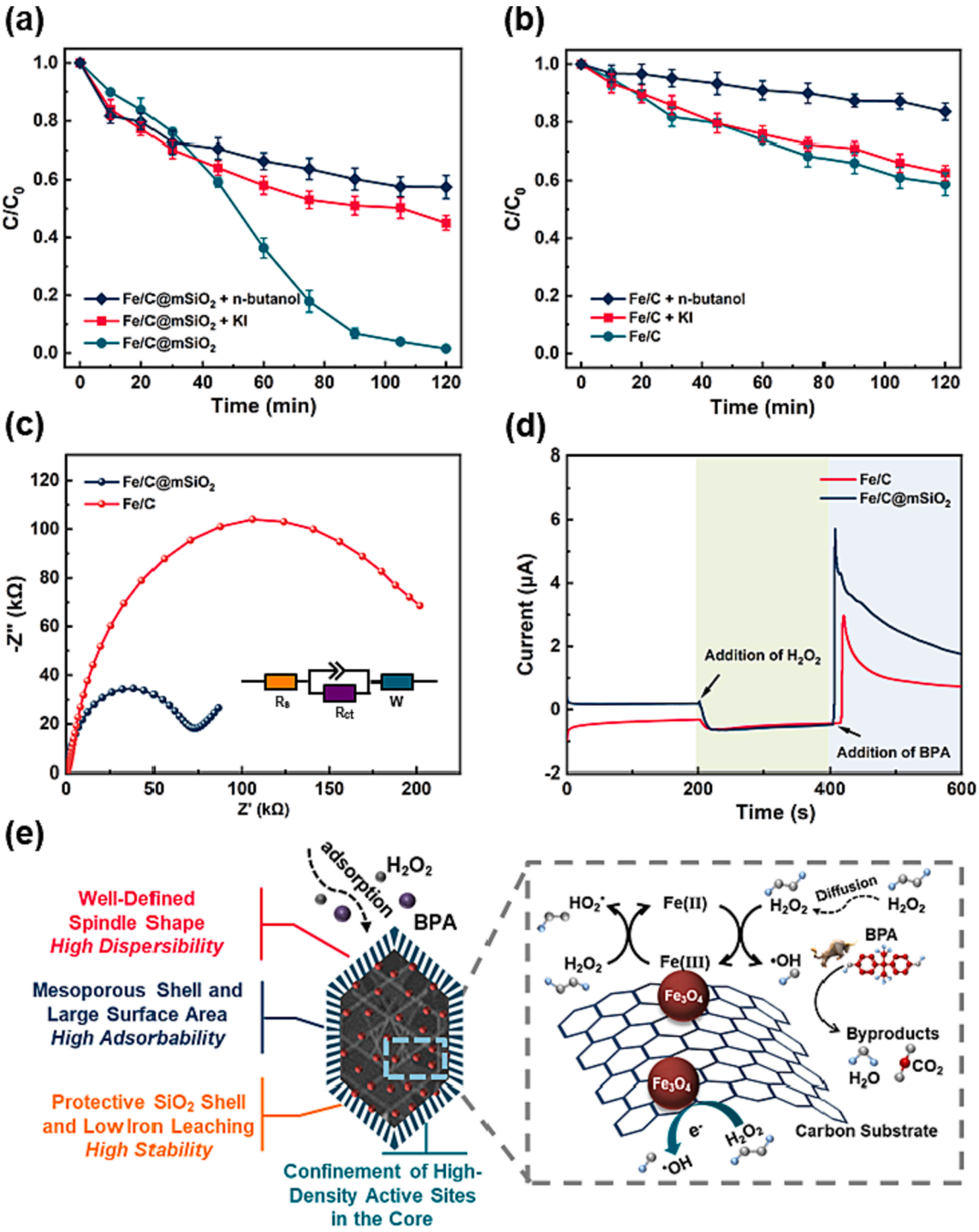

Fig. 7. Effect of radical scavengers on BPA decay in (a) Fe/C@mSiO$_2$ - and (b) Fe/C-catalyzed HEF treatment. General conditions (if applicable): [KI] = 10 mM; [n-butanol] = 300 mM; [BPA] = 0.11 mM; [catalyst] = 0.2 g L^{-1}; current = 100 mA; initial pH = 6.2; IrO$_2$-based anode. (c) EIS spectra obtained for Fe/C and Fe/C@mSiO$_2$ used as electrodes. (d) Chronoamperometry curves upon addition of H_2O_2 and BPA, using Fe/C and Fe/C@mSiO$_2$ as electrodes. (e) Proposed mechanism for the Fe/C@mSiO$_2$-catalyzed HEF degradation of BPA. In all cases, MOF pyrolysis made at 550 °C.

electron transfer [5]. The R_{ct} value of Fe/C@mSiO$_2$ was 78.6 kΩ, being much lower than that of Fe/C (162.0 kΩ), demonstrating the improved electron transfer on Fe/C@mSiO$_2$ as a result of presence of the SiO$_2$ shell. Similarly, the Tafel slopes from the polarization curves obtained with Fe/C@mSiO$_2$ and Fe/C were 160.6 and 248.6 mV dec^{-1}, respectively (Fig. S7). The much lower Tafel slope of the former corroborates the faster electron transfer rate [10]. Finally, the chronoamperometric responses were recorded to discern the electrical signals generated by the electron transfer occurring during the Fe/C@mSiO$_2$- or Fe/C-catalyzed HEF treatment of BPA (Fig. 7d). The current output was dramatically enhanced upon H_2O_2 injection in the case of Fe/C@mSiO$_2$, suggesting that H_2O_2 can adsorb on the surface of catalyst to react at the iron sites at the established potential. After the addition of BPA, a current spike was observed due to the fast electron transfer from BPA to the catalyst surface, implying that efficient electron transfer is feasible at the catalyst [10,70]. Worth highlighting, the intensities of the current responses with Fe/C catalyst are obviously weaker. In conclusion, the greater electron transfer ability of Fe/C@mSiO$_2$ enabled fast activation

of H_2O_2 to produce more $^{\bullet}OH$, justifying its better catalytic performance in HEF.

Based on the above results, a detailed mechanism for BPA degradation by Fe/C@mSiO$_2$-catalyzed HEF system has been proposed in Fig. 7e. First, the as-prepared Fe/C@mSiO$_2$ inherits many advanced properties of the MIL-88B(Fe) precursor, such as the tailored morphology and the uniformly dispersed iron active sites, whereas the organic ligands give rise to defect-rich carbon substrate that facilitates the adsorption of BPA and the electron transfer during the reactions. The introduction of a mesoporous SiO_2 shell yields a nanoreactor with increased specific surface area that protects the core catalyst from severe collapse in water, and the shell favors the rapid diffusion of BPA to the core sites. Meanwhile, the adsorbed H_2O_2 is activated by the iron active sites in the core to generate $^{\bullet}OH$. Both BPA and $^{\bullet}OH$ are confined within the microenvironment induced by the core–shell structure, leading to a higher collision probability. The efficient degradation of BPA releases the occupied adsorption sites to further adsorb residual BPA.

4. Conclusions

A Fe/C@mSiO$_2$ core–shell nanoreactor with abundant inner iron active sites and protective mesoporous SiO_2 shell was synthesized using an MIL-88B(Fe) precursor. The unique structure of MIL-88B(Fe) ensured the high dispersibility and density of iron active sites in the resulting carbonaceous matrix. The rigid mSiO$_2$ shell not only slowed down the deactivation of the iron active sites, but it also provided porous and permeable channels to enhance the mass transport. The Fe/C@mSiO$_2$-catalyzed HEF achieved the complete abatement of BPA, with extremely low iron leaching, being superior to HEF with other catalysts. The efficient removal of BPA and other target organic micropollutants is viable at near-neutral pH, showing an excellent catalyst reuse. The mechanistic investigation revealed that the core–shell structure boosts the both mass transport and electron transfer during HEF treatment, thus facilitating the degradation.

CRediT authorship contribution statement

Jingwen Wang: Conceptualization, Data curation, Investigation, Validation. **Hao Li:** Conceptualization, Investigation, Supervision. **Pan Xia:** Formal analysis, Investigation. **Huanbin Liu:** Formal analysis, Investigation. **Xi Chen:** Data curation, Investigation. **Zhihong Ye:** Conceptualization, Funding acquisition, Investigation, Methodology, Project administration, Resources, Supervision, Writing – original draft, Writing – review & editing. **Qiang He:** Resources, Supervision. **Ignasi Sirés:** Funding acquisition, Methodology, Project administration, Resources, Supervision, Writing – original draft, Writing – review & editing.

Declaration of competing interest

The authors declare that they have no known competing financial interests or personal relationships that could have appeared to influence the work reported in this paper.

Data availability

Data will be made available on request.

Acknowledgments

The authors gratefully acknowledge financial support from the National Natural Science Foundation of China (No. 52100073), the PhD Gateway Program of Chongqing, (CSTB2022BSXM-JCX0140), the Natural Science Foundation of Chongqing, (CSTB2022NSCQ-MSX0432), the Venture and Innovation Support Program for Chongqing Over–seas Returnees (cx2022048), as well as projects PID2019-109291RB-I00, PID2022-140378OB-I00 and PDC2022-133624-I00 (MCIN/AEI/10.13039/501100011033, Spain) with co-funding from the EU.

Appendix A. Supplementary data

Supplementary data to this article can be found online at https://doi.org/10.1016/j.cej.2024.149230.

References

[1] S.O. Ganiyu, M.H. Zhou, C.A. Martínez-Huitle, Heterogeneous electro-Fenton and photoelectro-Fenton processes: a critical review of fundamental principles and application for water/wastewater treatment, Appl. Catal. B: Environ. 235 (2018) 103–129.
[2] H. Monteil, Y. Péchaud, N. Oturan, M.A. Oturan, A review on efficiency and cost effectiveness of electro- and bio-electro-Fenton processes: application to the treatment of pharmaceutical pollutants in water, Chem. Eng. J. 376 (2019) 119577.
[3] C.A. Martínez-Huitle, M.A. Rodrigo, I. Sirés, O. Scialdone, A critical review on latest innovations and future challenges of electrochemical technology for the abatement of organics in water, Appl. Catal. B: Environ. 328 (2023) 122430.
[4] P. Xia, C. Wang, Q. He, Z. Ye, I. Sirés, MOF-derived single-atom catalysts: The next frontier in advanced oxidation for water treatment, Chem. Eng. J. 452 (2023) 139446.
[5] V. Melin, P. Salgado, A. Thiam, A. Henríquez, H.D. Mansilla, J. Yáñez, C. Salazar, tudy of degradation of amitriptyline antidepressant by different electrochemical advanced oxidation processes, Chemosphere 274 (2021) 129683.
[6] P. Xia, Z. Ye, L. Zhao, Q. Xue, S. Lanzalaco, Q. He, X.Q.I. Sirés, Tailoring single-atom FeN_4 moieties as a robust heterogeneous catalyst for high-performance electro-Fenton treatment of organic pollutants, Appl. Catal. B: Environ. 322 (2023) 122116.
[7] Z. Ye, E. Brillas, F. Centellas, P.L. Cabot, I. Sirés, Electro-Fenton process at mild pH using Fe(III)-EDDS as soluble catalyst and carbon felt as cathode, Appl. Catal. B: Environ. 257 (2019) 117907.
[8] O.M. Cornejo, F.J. Piña, J.L. Nava, Hybrid water treatment flow plant using hydrogen peroxide-based electro-activated persulfate and photoelectro-Fenton processes: The combustion of Reactive Orange 16 dye, J. Ind. Eng. Chem. 124 (2023) 558–569.
[9] I. Sirés, E. Brillas, Upgrading and expanding the electro-Fenton and related processes, Curr. Opinion Electrochem. 27 (2021) 100686.
[10] Z. Ye, W. Zhang, S. Lanzalaco, L. Zhao, I. Sirés, P. Xia, J. Zhai, Q. He, Ultra-uniform MIL-88B(Fe)/Fe_3S_4 hybrids engineered by partial sulfidation to boost catalysis in electro-Fenton treatment of micropollutants: Experimental and mechanistic insights, Chem. Eng. J. 455 (2023) 140757.
[11] F. Deng, H. Olvera-Vargas, M. Zhou, S. Qiu, Ignasi Sirés, Enric Brillas, Critical review on the mechanisms of Fe^{2+} regeneration in the electro-Fenton process: Fundamentals and boosting strategies, Chem. Rev. 123 (2023) 4635–4662.
[12] Y. Xu, P. Xia, C. Wang, J. Cai, H. Li, Z. Ye, H. Zhang, A mini-review on MOFs activated peroxide processes and the enhancement with the external energy, Chem. Eng. J. 462 (2023) 142021.
[13] C. Wang, J. Kim, V. Malgras, J. Na, J. Lin, J. You, M. Zhang, J. Li, Y. Yamauchi, Metal-organic frameworks and their derived materials: Emerging catalysts for a sulfate radicals-based advanced oxidation process in water purification, Small 15 (2019) 1900744.
[14] Y. Li, B. Yao, Y. Chen, Y. Zhou, X. Duan, Metal-organic frameworks (MOFs) as efficient catalysts for electro-Fenton (EF) reactions: Current progress and prospects, Chem. Eng. J. 463 (2023) 142287.
[15] T. Hu, L. Tang, H. Feng, J. Zhang, X. Li, Y. Zuo, Z. Lu, W. Tang, Metal-organic frameworks (MOFs) and their derivatives as emerging catalysts for electro-Fenton process in water purification, Coordin. Chem. Rev. 451 (2022) 214277.
[16] X. Du, S. Wang, F. Ye, Z. Qingrui, Derivatives of metal-organic frameworks for heterogeneous Fenton-like processes: From preparation to performance and mechanisms in wastewater purification - A mini review, Environ. Res. 206 (2022) 112414.
[17] W. Xiao, M. Cheng, Y. Liu, J. Wang, G. Zhang, Z. Wei, L. Li, L. Du, G. Wang, H. Liu, Functional metal/carbon composites derived from metal-organic frameworks: Insight into structures, properties, performances, and mechanisms, ACS. Catal. 13 (2023) 1759–1790.
[18] L. Yu, H.B. Wu, X.W.D. Lou, Self-templated formation of hollow structures for electrochemical energy applications, Acc. Chem. Res. 50 (2017) 293–301.
[19] Z. Wang, Y. Du, P. Zhou, Z. Xiong, C. He, Y. Liu, H. Zhang, G. Yao, B. Lai, Strategies based on electron donors to accelerate Fe(III)/Fe(II) cycle in Fenton or Fenton-like processes, Chem. Eng. J. 454 (2023) 140096.
[20] Z. Ye, J.A. Padilla, E. Xuriguera, E. Brillas, I. Sirés, Magnetic MIL(Fe)-type MOF-derived N-doped nano-ZVI@C rods as heterogeneous catalyst for the electro-Fenton degradation of gemfibrozil in a complex aqueous matrix, Appl. Catal. B: Environ. 266 (2022) 118604.
[21] K. Xu, K. Cui, C. Li, M. Cui, R. Weerasooriya, X. Li, Z. Ding, Xing Chen, Magnetic core-shell-structured FeO_x/CN catalyst mediated peroxymonosulfate activation for degradation of 2,4-dichlorophenol via non-radical pathway, ACS ES&T Water 1 (2021) 2217–2232.
[22] S. Cheng, H. Zheng, C. Shen, B. Jiang, F. Liu, A. Li, Hierarchical iron phosphides composite confined in ultrathin carbon lyer as effective heterogeneous electro-

Fenton catalyst with prominent stability and catalytic activity, Adv. Funct. Mater. 31 (2021) 2106311.
[23] Y. Zhou, Y. Li, Y. Hou, C. Wang, Y. Yang, J. Shang, X. Cheng, Core-shell catalysts for the elimination of organic contaminants in aqueous solution: A review, Chem. Eng. J. 455 (2023) 140604.
[24] S. Pan, X. Guo, X. Lu, R. Li, H. Hu, X. Nie, B. Liu, R. Chen, M. Zhu, S. Hei, X. Zhu, S. Zhang, H. Zhou, Boosting peroxymonosulfate activation by a novel bifunctional core-shell nanoreactor $MnFe_2O_4$@HZO for nitrilotris-methylenephosphonic acid removal, Appl. Catal. B: Environ. 330 (2023) 122508.
[25] C. Zhu, S. Zhao, Z. Fan, H. Wu, F. Liu, Z. Chen, A. Li, Confinement of CoP nanoparticles in nitrogen-doped yolk-shell porous carbon polyhedron for ultrafast catalytic oxidation, Adv. Funct. Mater. 30 (2020) 2003947.
[26] S. Zhang, H. Gao, X. Xu, R. Cao, H. Yang, X. Xu, J. Li, MOF-derived CoN/N-C@SiO_2 yolk-shell nanoreactor with dual active sites for highly efficient catalytic advanced oxidation processes, Chem. Eng. J. 381 (2020) 122670.
[27] C. Gao, S. Chen, X. Quan, H. Yu, Y. Zhang, Enhanced Fenton-like catalysis by iron-based metal organic frameworks for degradation of organic pollutants, J. Catal. 356 (2017) 125–132.
[28] M. Ahmad, X. Quan, S. Chen, H. Yu, Tuning Lewis acidity of MIL-88B-Fe with mix-valence coordinatively unsaturated iron centers on ultrathin Ti_3C_2 nanosheets for efficient photo-Fenton reaction, Appl. Catal. B: Environ. 264 (2010) 118534.
[29] C. Zhao, L. Meng, H. Chu, J.F. Wang, T. Wang, Y. Ma, C.C. Wang, Ultrafast degradation of emerging organic pollutants via activation of peroxymonosulfate over Fe_3C/Fe@N-C-x: Singlet oxygen evolution and electron-transfer mechanisms, Appl. Catal. B: Environ. 321 (2021) 122034.
[30] S. Li, J. Huang, K. Yi, H. Pang, Z. Liu, W. Zhang, C. Zhang, S. Liu, J. Li, C. Liu, W. Shu, Silica reinforced core-shell quorum quenching beads to control biofouling in an MBR, Chem. Eng. J. 460 (2023) 141725.
[31] T. Yang, D. Yu, D. Wang, T. Yang, Z. Li, M. Wu, M. Petru, J. Crittenden, Accelerating Fe(III)/Fe(II) cycle via Fe(II) substitution for enhancing Fenton-like performance of Fe-MOFs, Appl. Catal. B: Environ. 286 (2021) 119859.
[32] S. Bao, J. Li, B. Guan, M. Jia, O. Terasaki, J. Yu, A green selective water-etching approach to MOF@mesoporous SiO_2 yolk-shell nanoreactors with enhanced catalytic stabilities, Matter 3 (2022) 498–508.
[33] Y. Zhang, G. Daniel, S. Lanzalaco, A.A. Isse, A. Facchin, A. Wang, E. Brillas, C. Durante, I. Sirés, H_2O_2 production at gas-diffusion cathodes made from agarose derived carbons with different textural properties for acebutolol degradation in chloride media, J. Hazard. Mater. 423 (2022) 127005.
[34] X. Li, X. Yan, X. Hu, R. Feng, M. Zhou, Yolk-shell ZIFs@SiO_2 and its derived carbon composite as robust catalyst for peroxymonosulfate activation, J. Environ. Manage. 262 (2020) 110299.
[35] S. Nemec, S. Kralj, A Versatile interfacial coassembly method for fabrication of tunable silica shells with radially aligned dual mesopores on diverse magnetic core nanoparticles, ACS Appl. Mater. Inter. 13 (2021) 1883–1894.
[36] W. Xie, L. Gu, X. Sun, M. Liu, S. Li, Q. Wang, D. Liu, D. He, Ferrocene derived core-shell structural Fe_3O_4@C nanospheres for superior lithium storage properties, Electrochim. Acta. 220 (2016) 107–113.
[37] M. Ren, M. Yang, W. Liu, M. Li, L. Su, C. Qiao, X. Wu, H. Ma, Ultra-small Fe_3O_4 nanocrystals decorated on 2D graphene nanosheets with excellent cycling stability as anode materials for lithium ion batteries, Electrochim. Acta. 194 (2016) 219–227.
[38] H. Liu, S. Luo, D. Hu, X. Liu, Q. Wang, Z. Wang, Y. Wang, L. Chang, Y. Liu, T. Yi, Y. Zhang, A. Hao, Design and synthesis of carbon-coated α-Fe_2O_3@Fe_3O_4 heterostructured as anode materials for lithium ion batteries, Appl. Surf. Sci. 495 (2019) 143590.
[39] X. Yang, Y. Zhou, H. Xing, H. Wang, W. Feng, J. Feng, X. Zhu, Z. Shi, Y. Zong, X. Li, MIL-88B (Fe) driven Fe/Fe_3C encapsulated in high-crystalline carbon for high-efficient microwave absorption and electromagnetic interference shielding, J. Phys. d: Appl. Phys. 55 (2022) 145003.
[40] X. Xu, F. Ran, H. Lai, Z. Cheng, T. Lv, L. Shao, Y. Liu, In situ confined bimetallic metal-organic framework derived nanostructure within 3D interconnected bamboo-like carbon nanotube networks for boosting electromagnetic wave absorbing performances, ACS Appl. Mater. Interfaces 11 (2019) 35999–36009.
[41] X. Gong, J. Zhu, J. Li, R. Gao, Q. Zhou, Z. Zhang, H. Dou, L. Zhao, X. Sui, J. Cai, Y. Zhang, B. Liu, Y. Hu, A. Yu, S. Sun, Z. Wang, Z. Chen, Self-templated hierarchically porous carbon nanorods embedded with atomic Fe-N_4 active sites as efficient oxygen reduction electrocatalysts in Zn-Air batteries, Adv. Funct. Mater. 31 (2020) 2008085.
[42] S. Zhang, Y. Zhuo, C.I. Ezugwu, C. Wang, C. Li, S. Liu, Synergetic molecular oxygen activation and catalytic oxidation of formaldehyde over defective MIL-88B(Fe) nanorods at room temperature, Environ. Sci. Technol. 55 (2021) 8341–8350.
[43] H. Peng, W. Xiong, Z. Yang, J. Tong, M. Jia, Y. Xiang, S. Sun, Z. Xu, Fe_3O_4-supported N-doped carbon channels in wood carbon form etching and carbonization: Boosting performance for persulfate activating, Chem. Eng. J. 457 (2023) 141317.
[44] D. Gu, Y. Liu, H. Zhu, Y. Gan, B. Zhang, W. Yang, J. Hao, Magnetic porphyrin-based metal organic gel for rapid RhB removal and enhanced antibacterial activity by heterogeneous photo-Fenton reaction under visible light, Chemosphere 303 (2022) 135114.
[45] F. Wang, H. Fu, F. Wang, X. Zhang, P. Wang, C. Zhao, C. Wang, Enhanced catalytic sulfamethoxazole degradation via peroxymonosulfate activation over amorphous CoS_x@SiO_2 nanocages derived from ZIF-67, J. Hazard. Mater. 423 (2022) 126998.
[46] K. Li, J. Feng, X. Hao, X. Song, C. Zhang, P. Ning, K. Li, Catalytic oxidation mechanism of AsH_3 over CuO@SiO_2 core-shell catalysts via experimental and theoretical studies, J. Hazard. Mater. 443 (2023) 130318.
[47] Y. Zhang, Y. Mei, S. Ma, Y. Yang, X. Deng, Y. Guan, T. Zha, B. Jiang, T. Yao, Q. Yang, J. Wu, A simple and green method to prepare non-typical yolk/shell nanoreactor with dual-shells and multiple-cores: Enhanced catalytic activity and stability in Fenton-like reaction, J. Hazard. Mater. 436 (2022) 129234.
[48] M. Zhang, C. Wang, C. Liu, R. Luo, J. Li, X. Sun, J. Shen, W. Han, L. Wang, Metal-organic framework derived Co_3O_4/C@SiO_2 yolk-shell nanoreactors with enhanced catalytic performance, J. Mater. Chem. A 6 (2018) 11226–11235.
[49] A. Cherevotan, B. Ray, S.R. Churipard, K. Kaur, U.K. Gautam, C.P. Vinod, S. C. Peter, Influence of support textural property on CO_2 to methane activity of Ni/SiO_2 catalysts, Appl. Catal. B: Environ. 317 (2022) 121692.
[50] T. Van Tran, D.T.C. Nguyen, H.T.N. Le, L.G. Bach, D.N. Vo, T.T. Dao, K.T. Lim, T. D. Nguyen, Effect of thermolysis condition on characteristics and nonsteroidal anti-inflammatory drugs (NSAIDs) absorbability of Fe-MIL-88B-derived mesoporous carbons, J Environ Chem Eng. 7 (2019) 103356.
[51] M. Ahmad, X. Quan, S. Chen, H. Yu, Tuning Lewis acidity of MIL-88B-Fe with mix-valence coordinatively unsaturated iron centers on ultrathin Ti_3C_2 nanosheets for efficient photo-Fenton reaction, Appl. Catal. B: Environ. 264 (2020) 118534.
[52] M. Li, Z. Zhang, G. Song, M.A. Nawaz, Z. Wang, Z. Chen, D. Liu, Surface Si decoration of ultrafine NaFeMn-Si catalyst enabling high Fe-phase electron density for effectively converting syngas to aromatics, Chem. Eng. J. 433 (2022) 134599.
[53] J. Han, X. Meng, L. Lu, J. Bian, Z. Li, C. Sun, Single-atom Fe-N_x-C as an efficient electrocatalyst for zinc-air batteries, Adv. Funct. Mater. 29 (2019) 1808872.
[54] T. Wang, H. Zhang, Y. Liu, L. Zhang, B. Xing, Ultrathin porous carbon nanosheet as an efficient adsorbent for the removal of bisphenol A: The overlooked role of topological defects, Chemosphere 306 (2022) 135549.
[55] X. Du, W. Fu, P. Su, J. Cai, M. Zhou, Internal-micro-electrolysis-enhanced heterogeneous electro-Fenton process catalyzed by Fe/Fe_3C@PC core-shell hybrid for sulfamethazine degradation, Chem. Eng. J. 398 (2020) 125681.
[56] Y. Li, C. Zeng, C. Wang, L. Zhang, Preparation of C@silica core/shell nanoparticles from ZIF-8 for efficient ciprofloxacin adsorption, Chem. Eng. J. 340 (2018) 645–653.
[57] Z. Ye, R. Oriol, C. Yang, I. Sirés, X. Li, A novel NH_2-MIL-88B(Fe)-modified ceramic membrane for the integration of electro-Fenton and filtration processes: A case study on naproxen degradation, Chem. Eng. J. 433 (2022) 133547.
[58] H. Zhang, X. Gong, Z. Song, S. Zhang, W. Du, T.T. Nguyen, M. Guo, X. Gao, Wood-based carbon quantum dots for enhanced photocatalysis of MIL-88B(Fe), Opt. Mater. 113 (2021) 110865.
[59] M. Zhang, R. Luo, C. Wang, W. Zhang, X. Yan, X. Sun, L. Wang, J. Li, Confined pyrolysis of metal-organic frameworks to N-doped hierarchical carbon for non-radical dominated advanced oxidation processes, J. Mater. Chem. A 7 (2019) 12547–12555.
[60] S. Zhang, X. Xu, G. Zhang, J. Bin Liu Yang, One-pot one-step synthesis of Au@SiO_2 core-shell nanoparticles and their shell-thickness-dependent fluorescent properties, RSC Adv. 9 (2019) 17674.
[61] H. Fu, Y. Guo, J. Yu, J. Shen, Y. Zhao, Y. Xie, S. Ling, S. Ouyang, W.Z. Li, Tuning the shell thickness of core-shell α-Fe_2O_3@SiO_2 nanoparticles to promote microwave absorption, Chinese Chem. Lett. 33 (2022) 957–962.
[62] H. Yu, W. Wang, M. Liu, T. Zhao, R. Lin, M. Hou, Y. Kou, L. Chen, A.A. Elzatahry, F. Zhang, D. Zhao, X. Li, Versatile synthesis of dendritic mesoporous rare earth-based nanoparticles, Sci Adv. 8 (2022) 2356.
[63] Z. Ye, G.E.M. Schukraft, A. L'Hermitte, Y. Xiong, E. Brillas, C. Petit, I. Sirés, Mechanism and stability of an Fe-based 2D MOF during the photoelectro-Fenton treatment of organic micropollutants under UVA and visible light irradiation, Water Res. 184 (2020) 115986.
[64] H. Olvera-Vargas, N. Gore-Datar, O. Garcia-Rodriguez, S. Mutnuri, O. Lefebvre, Electro-Fenton treatment of real pharmaceutical wastewater paired with a BDD anode: reaction mechanisms and respective contribution of homogeneous and heterogeneous $^{\bullet}$OH, Chem. Eng. J. 404 (2021) 126524.
[65] G. Wang, K. Wang, Z. Liu, Y. Feng, S. Yang, Y. Su, X. Qian, Pe. Jin, J. Wei, Hollow multi-shelled NiO nanoreactor for nanoconfined catalytic degradation of organic pollutants via peroxydisulfate activation, Appl. Catal. B: Environ. 325 (2023) 122359.
[66] J.D.S. Salla, K.D.B. Martinello, G.L. Dotto, E. García-Díaz, H. Javed, P.J.J. Alvarez, E.L. Foletto, Synthesis of citrate-modified $CuFeS_2$ catalyst with significant effect on the photo-Fenton degradation efficiency of bisphenol A under visible light and near-neutral pH, Colloids Surf. A Physicochem. Eng. Asp. 595 (2020) 124679.
[67] X. Luo, S. Yu, D. Xu, J. Ding, X. Zhu, J. Xing, T. Wu, X. Zheng, T.M. Aminabhavi, X. Cheng, H. Liang, Isoporous catalytic ceramic membranes for ultrafast contaminants elimination through boosting confined radicals, Chem. Eng. J. 455 (2023) 140872.
[68] M. Tamtaji, M. Kazemeini, Enhanced singlet oxygen production under nanoconfinement using silica nanocomposites towards improving the photooxygenation's conversion, J. Nanopart. Res. 24 (2022) 174.
[69] H. Qin, R. Xiao, W. Shi, Y. Wang, H. Li, L. Guo, H. Cheng, J. Chen, Magnetic core–shell-structured Fe_3O_4@CeO_2 as an efficient catalyst for catalytic wet peroxide oxidation of benzoic acid, RSC Adv. 8 (2018) 17674.
[70] Y. Li, C. Wang, F. Wang, W. Liu, L. Chen, C. Zhao, H. Fu, P. Wang, X. Duan, Nearly zero peroxydisulfate consumption for persistent aqueous organic pollutants degradation via nonradical processes supported by in-situ sulfate radical regeneration in defective MIL-88B(Fe), Appl. Catal. B: Environ. 331 (2023) 122699.